

New links between invariant dynamical structures and uncertainty quantification.

Guillermo García-Sánchez,^{1,2} Ana Maria Mancho,¹ Makrina Agaoglou,³ and Stephen Wiggins^{4,5}

¹*Instituto de Ciencias Matemáticas, CSIC, C/Nicolas Cabrera 15, Campus Cantoblanco, Madrid, 28049, Spain*

²*Escuela Técnica Superior de Ingenieros de Telecomunicación,*

Universidad Politécnica de Madrid, Av. Complutense, 30, Madrid, 28040, Spain

³*Departamento de Matemática Aplicada a la Ingeniería Industrial,*

Escuela Técnica Superior de Ingenieros Industriales,

Universidad Politécnica de Madrid, c/ José Gutiérrez Abascal, 2, Madrid, 28006, Spain

⁴*School of Mathematics, University of Bristol, Fry Building,*

Woodland Road, Bristol, BS8 1UG, United Kingdom.

⁵*Department of Mathematics, United States Naval Academy,*

Chauvenet Hall, 572C Holloway Road, Annapolis, MD 21402-5002

This paper proposes a new uncertainty measure, appropriate for quantifying the performance of transport models in assessing the origin or source of a given observation. It is found that in a neighbourhood of the observation the proposed uncertainty measure is related to the invariant dynamical structures of the model. The paper illustrates the implementation of the proposed definition to quantify the performance of ocean data sets in the context of a real oil spill event in the Eastern Mediterranean in 2021.

I. INTRODUCTION

Models in real-world applications are subjected to uncertainty in their results, and this is particularly notorious in models that describe the ocean or the atmosphere state. In these geophysical contexts, the availability of tools that quantify the uncertainty of model outputs is very much desired as this allows the evaluation of their reliability and the assessment of their use in real applications. Uncertainty quantification is a very broad question and it has been addressed from different perspectives. One approach to this problem involves performing a sensitivity analysis, which determines what inputs in the model, which typically is a partial differential equation, affect the outputs the most. A related issue, referred to as forward propagation of uncertainty, consists of examining how uncertainty in the model parameter inputs affects uncertainty in the model outputs. In this framework it may happen that experimental data are available. In this case, it is possible to infer the set of parameters that better fit the outputs for the proposed model. This setting can be precisely formulated as a Bayesian inverse problem, which for a given observation, and an assumed noise model, determines the parameters that are most likely to have produced the data. Typically, Bayesian analyses provide the framework for many inverse uncertainty quantification applications [1, 2]. These methods employ Bayesian inference theory along with exploring the posterior probability density function (PDF) by Markov Chain Monte Carlo (MCMC) sampling. Other methods include statistical methods based on maximum likelihood estimation (MLE) [3] and data assimilation methods. Data assimilation methods combine experimental observations with code predictions and their respective errors to provide an improved estimate of the system state and of the associated uncertainty [4]. All of these approaches assume that the model is known, with undetermined parameters, and perform adaptations on the model inputs. However, there is a different type of problem for which only an approximate model is available and its exact expression is unknown. We delve into an explanation of such problems.

Recently, García-Sánchez et al. [5] have proposed to quantify uncertainty associated with transport by currents in settings in which the exact model connecting two successive observations (or the currents producing the observed transport) was not known. They have quantified uncertainty motivated by the need to judge the performance of ocean model outputs to describe oil spill events such as that described in [6]. In this reported event an identified spill occurs at a certain time and it is required to describe its evolution to determine if it will affect critical areas, and there is a need to assess ocean models to this end. García-Sánchez et al. [5] approach evaluates the reliability of the ocean currents with respect to the transport that they produce. Indeed, transport in the ocean surface is produced by fluid parcels that follow trajectories $\mathbf{x}(t)$ that evolve according to the dynamical system:

$$\frac{d\mathbf{x}}{dt} = \mathbf{v}(\mathbf{x}, t), \quad (1)$$

This system is a nonlinear non-autonomous dynamical system in which there are uncertainties in the velocities $\mathbf{v}(\mathbf{x}, t)$, because they are not exactly known given that they come from solving highly sensitive partial differential equations. This is what we mean by *not knowing* the exact problem: the right-hand side of Equation (1) is only an approximation. Typically, in other problems where uncertainty has been studied, the system obeys an explicitly known partial differential equation where the unknowns are not within the model itself but rather in adjustable parameters of

the equation or in the observations. However, our case is of a different nature because the right-hand side of Eq. (1) is a key part of the equation and not exactly known. The uncertainties in the velocities $\mathbf{v}(\mathbf{x}, t)$ produce uncertainties in the solutions $\mathbf{x}(t)$. García-Sánchez et al. [5] quantified this type of uncertainty by means of error measures in settings where the initial observation was known, \mathbf{x}_0 , and a target state at a later final time, \mathbf{x}^* . This approach was adequate to quantify the suitability of the model given in Eq. (1) to represent this sequence of observations in forward time. In doing so they found links between the uncertainty and the stable invariant manifolds of hyperbolic trajectories present in the system (1).

This paper aims to complete the described picture as follows. While results in [5] consider the uncertainty of a model based on ocean currents in order to describe the final fate of an observation as it evolves *forward* in time, the new setting considers the uncertainty of a similar model in order to identify the original location of an observation in a *past* time, once the position, \mathbf{x}_1 , of this observation is known at the present time. In a nutshell, previous results were about: where do trajectories end up? How could it be measured if they are consistently described by a model constructed from approximate velocities? Now the results we desire are about: where do trajectories come from? how could it be measured if their origin is consistently described by a model that is constructed from approximate velocities? In this context, this paper provides a new approach to measuring uncertainty using errors adequate for the backward time setting. We find that similar to what was found in García-Sánchez et al. [5], this uncertainty has a *structure* in a neighborhood of the observation \mathbf{x}_1 , and this structure is related to the unstable invariant manifolds of the hyperbolic trajectories present in the vector field of equation (1).

Once this new type of uncertainty is introduced, we proceed to assess ocean data capabilities in real events that demand this type of perspective. In particular, a recent contamination event that occurred in 2021 in the Eastern Mediterranean is considered. Specifically in this event, thoroughly described in [7], several beaches were affected by a spill of unknown origin. In contrast to the results by [5], now observations are done at the arrival point and the identification of their source is the goal. Equipped with the new tool we describe in detail its use to quantify the performance of different ocean data sets for describing observations adequately. There are other attempts to identify the best dataset for predicting the drift of oil spills [8, 9]. However, their approach consists of using uncertainty estimators in forward time.

In summary, the goal of this article is to propose a new uncertainty measure appropriate for quantifying the suitability of a model to describe the origin of trajectories. It is found that the considered uncertainty has a structure correlated with the unstable manifolds of the hyperbolic trajectories of the model. The capacity of this new measure is exploited for characterizing the performance of ocean data sets in real events. Accordingly, the structure of this article is as follows. Section 2 provides a new definition for uncertainty quantification suitable to describe the new setting and, in a simple example, discusses links with unstable manifolds of hyperbolic trajectories. Section 3 presents the application of this tool to the mentioned oil spill event that affected the Eastern Mediterranean, and shows how it helps to discriminate between two data sets, and supports the identification of the most suitable one for searching the spill source. In Section 4, the paper concludes with a discussion of the implications and potential applications of this approach.

II. UNCERTAINTY QUANTIFICATION IN BACKWARD TIME

This section is focused on proposing a new definition of uncertainty quantification to describe the uncertainty in the origin or source of certain observations based on predictions by a model constructed from velocities. This section is limited to present the definition and to discuss its implementation in one simple example. This simplified scenario enables us to establish connections between the new definition of uncertainty and the unstable manifolds of hyperbolic trajectories. The objective, however, is to apply this definition to distinguish the most appropriate velocity field among various options, the one that best matches the observations.

We start by recalling results reported in [5] in the context of the simple example illustrated in Figure 1. Panel a) within this figure shows an initial observation, \mathbf{x}_0 , at time t_0 marked with a red circle. At a later time, t^* , this observation is at a target position, \mathbf{x}^* , marked with a red asterisk. This evolution is assumed to be following the model provided by Eq. (2), with a vector field in the background, which is represented at time t_0 , in the neighborhood of \mathbf{x}_0 and at time t^* in the neighborhood of \mathbf{x}^* . This vector field is chosen to be stationary, therefore its representation at later times, t^* , is the same as at t_0 . However, in general, this vector field will be time-dependent and therefore its representation at t^* is different from that at t_0 . The explicit expression for this vector field is:

$$\begin{cases} \frac{dx}{dt} = x, \\ \frac{dy}{dt} = -y, \end{cases} \quad (2)$$

This system has a stable manifold aligned with the vertical axis at $x = 0$ (blue line in Figure 1) and an unstable manifold aligned with the horizontal axis at $y = 0$ (red line in figure 1).

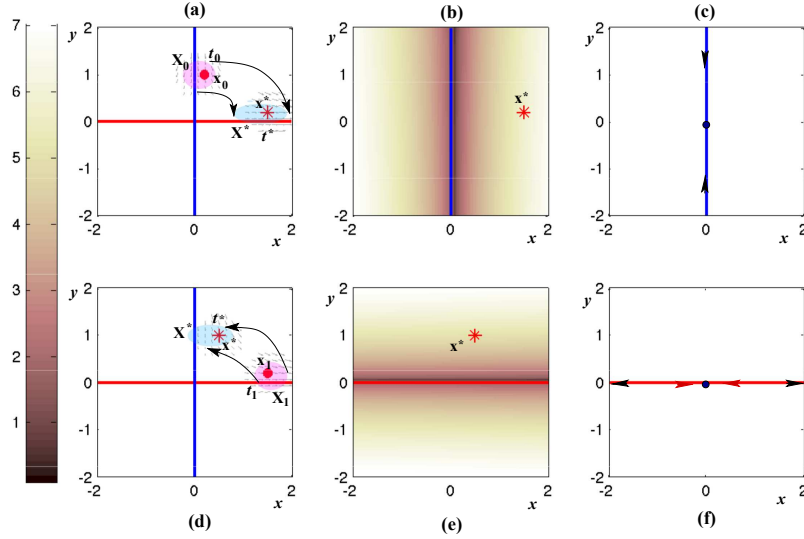


Figure 1. Panels a), b) and c) display a graphical representation of two sequential observations and their forward time evolution. a) The initial observation at time t_0 is expressed by the red circle with initial condition \mathbf{x}_0 . The final observed state \mathbf{x}^* at time t^* is referred to as the "target". In general, the evolution law linking these observations is unknown, but in our setting, it is approximated by Eq. (2), a system with a hyperbolic fixed point at the origin with stable and unstable manifolds in blue and red, respectively. The forward evolution of \mathbf{X}_0 (the pink blob) to \mathbf{X}^* (the light blue blob) according to this model is illustrated; b) a representation of L_{UQ} , in a domain beyond the neighbourhood X_0 for $\tau = 3$, where singular features are identified aligned with the stable manifold (in blue); c) a representation of the stable manifold. Black arrows point out the forward time evolution for initial condition on the stable manifold towards the fixed point at the origin; Panels d), e) and f) display a graphical representation of two sequential observations and their backward time evolution, d) the final observation at time t_1 is expressed with the red circle at the position \mathbf{x}_1 . Although both the origin and the model of this observation are unknown, its evolution is approached by Eq. (2), a system with a hyperbolic fixed point at the origin with stable and unstable manifolds in blue and red respectively. The backward evolution of \mathbf{X}_1 (the pink blob) to \mathbf{X}^* (the light blue blob) according to this model is illustrated; e) a representation of L_{BUQ} , in a domain beyond the neighborhood X_1 for $\tau = 3$, where singular features are identified aligned with the unstable manifold (in red); f) a representation of the unstable manifold. Red arrows point out the evolution in backward time towards the fixed point for initial conditions on the unstable manifold. Black arrows point out the evolution forward time moving away from the fixed point. The color bar at the top indicates a color scale for L_{UQ} and L_{BUQ} in panels b) and e).

García-Sánchez et al. [5] proposed several expressions to measure the error in a neighborhood \mathbf{X}_0 of \mathbf{x}_0 . Among those we consider this one:

$$L_{UQ}(\mathbf{X}_0, t_0, \tau, p) = \sum_{i=1}^n |x_i(t_0 + \tau) - x_i^*|^p, \quad p \leq 1, \quad \mathbf{X}_0 \in \mathbb{R}^n, \tau > 0. \quad (3)$$

Here, \mathbf{X}_0 represents a set of initial conditions whose coordinates (x_1, x_2, \dots, x_n) , belong to a n dimensional system (1) and are in the neighbourhood of the observation \mathbf{x}_0 . The coordinates of the target, towards which the system is assumed to evolve in a time interval τ , are $(x_1^*, x_2^*, \dots, x_n^*)$. Panel a) in Figure 1 illustrates the evolution from the set \mathbf{X}_0 (the pink blob) to \mathbf{X}^* (the light blue blob). Panel b) displays L_{UQ} evaluated in the whole domain. This representation expresses how much uncertainty would be associated with the system (2) beyond the neighborhood \mathbf{X}_0 , assuming that initial observations start at different points of the representation domain and that they evolve towards the assumed observed target position at the red asterisk in $\tau = 3$. It is clear from the representation, that L_{UQ} presents a structure that consists of singular features aligned with the stable manifold of the hyperbolic fixed point present in the vector field, as discussed and proven in [5].

In this paper, our interest is in quantifying the uncertainty of a model for identifying a target source \mathbf{x}^* , which is consistent with a later observation \mathbf{x}_1 at time t_1 . In this way, the target source, \mathbf{x}^* , is located at an earlier time $t^* = t_1 - \tau$. Similarly to the previous definition, for this setting, we propose the uncertainty to be:

$$L_{BUQ}(\mathbf{X}_1, t_1, \tau, p) = \sum_{i=1}^n |x_i(t_1 - \tau) - x_i^*|^p, \quad p \leq 1, \quad \mathbf{X}_0 \in \mathbb{R}^n, \tau > 0. \quad (4)$$

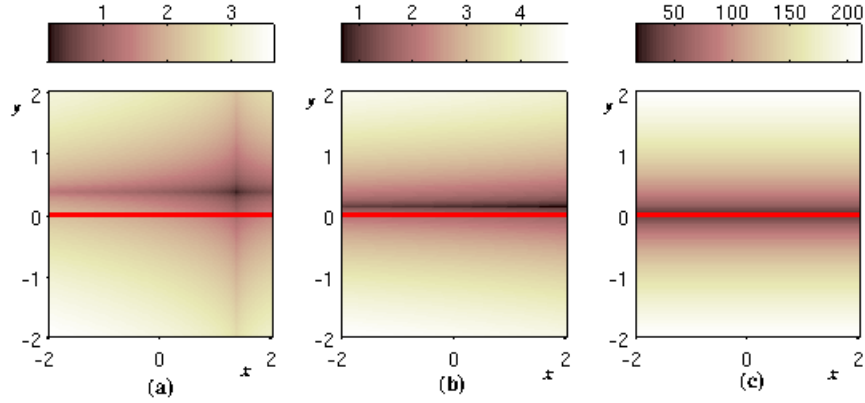


Figure 2. A representation in the plane of L_{BUQ} for the dynamical system (2) with target $\mathbf{x}^* = (0.5, 1)$. a) $\tau = 1$; b) $\tau = 2$; c) $\tau = 15$. The red line represents the position of the unstable manifold.

where now \mathbf{X}_1 represents a neighbourhood around the observation $\mathbf{x}_1 = (x_1, x_2, \dots, x_n)$ at time t_1 being n the dimension of the system (1), which in our specific examples is $n = 2$. The coordinates of the target are (x_1^*, x_2^*) , and uncertainty is provided in terms of a distance metric between the target and the *backward* evolution of points near to \mathbf{x}_1 for a period τ .

Panel d) in Figure 1 illustrates the backward in time evolution of \mathbf{X}_1 (the pink blob) to \mathbf{X}^* (the light blue blob) In the background, the panel also illustrates the vector field in a neighborhood of \mathbf{x}_1 at time t_1 , and in the neighborhood of \mathbf{x}^* at time t^* . Given that this vector field is stationary, its representation at an earlier time, $t^* = t_1 - \tau$, will be the same as at t_1 , although in general this vector field is time-dependent and therefore its representation at t^* is different from that at t_1 .

Panel e) displays in the whole domain, that is beyond the neighborhood \mathbf{X}_1 , L_{BUQ} evaluated for $p = 0.5$, assuming $\tau = 3$. This representation expresses how much uncertainty is associated to the system (2), assuming that observations \mathbf{x}_1 could be anywhere in the domain and that they have evolved there from the target position \mathbf{x}^* at $t^* = t_1 - \tau$. It is clear from the representation that L_{BUQ} presents a structure that consists of singular features aligned with the unstable manifold of the hyperbolic fixed point present in the vector field. A formal proof of this observation is given in the appendix. In the proof it is shown how a sufficiently large τ is required for the singular structures obtained from Eq. (4) to become aligned with the unstable manifolds. This is more clearly visualized in Figure 2. Panel a) shows the evaluation of L_{BUQ} for $\tau = 1$, where clearly the alignment with the unstable manifold is not yet achieved. Panels b) and c) confirm the convergence of the alignment towards the unstable manifold for, respectively, $\tau = 2$ and $\tau = 15$. This result completes the link between invariant dynamical structures and uncertainty quantification.

Panels c) and f) in Figure 1 graphically illustrate why the forward time uncertainty for system (2) is related to the stable manifold of the hyperbolic fixed point, while the backward time uncertainty is linked to the unstable manifold of that fixed point. Indeed, the forward time integration for initial conditions that stay on the stable manifold, for a sufficiently large τ , approach the fixed point at the origin, maintaining a fixed distance to the target, while all other initial conditions in the plane will increase their distance to the target for increasing τ . This is the origin of the singular features aligned with the stable manifold in forward time. Analogously, the backward time integration of initial conditions that stay on the unstable manifold, for a sufficiently large τ , approaches the fixed point at the origin, maintaining a fixed distance to the target. All other initial conditions in the plane will increase their distance to the target for increasing backward integration. This is the origin of the singular features aligned with the unstable manifold in backward time. Analogously this explanation also illustrates why both L_{UQ} and L_{BUQ} take minimum values along the unstable manifold. Indeed, they express the finite distance between the fixed point and the target, while the value of L_{UQ} and L_{BUQ} diverge for growing τ for all other points in the plane.

Figure 3 illustrates further these ideas. Panel a) represents the evolution versus τ of L_{UQ} at points: $(0,2)$ in red – which is on the stable manifold – and $(0,0)$ in black – the hyperbolic fixed point – as a function of τ , both with a target $\mathbf{x}^* = (1.5, 0.2)$ and $p = 0.5$. There is a transient behavior in τ for the point on the stable manifold, while in the limit of large τ both values converge to $|1.5|^{0.5} + |0.2|^{0.5} \sim 1.672$, which is the distance, in the defined metric, between the fixed point and the target. Similarly, panel b) represents the evolution of L_{BUQ} at points: $(2, 0)$ in red – which is on the unstable manifold – and $(0,0)$ in black – the hyperbolic fixed point – as a function of τ , both with a target $\mathbf{x}^* = (0.5, 1)$ and $p = 0.5$. In the limit of large τ , both converge to the constant ~ 1.71 .

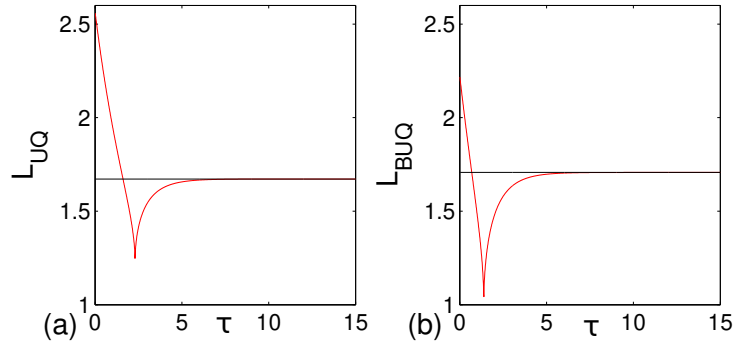


Figure 3. For the system given by Eq. (2), a) evolution of L_{UQ} versus τ on the fixed point (black line) and on a point on the stable manifold (red line) with target $\mathbf{x}^* = (1.5, 0.2)$; b) evolution of L_{BUQ} versus τ on the fixed point (black line) and on a point on the unstable manifold (red line) with target $\mathbf{x}^* = (0.5, 1)$.

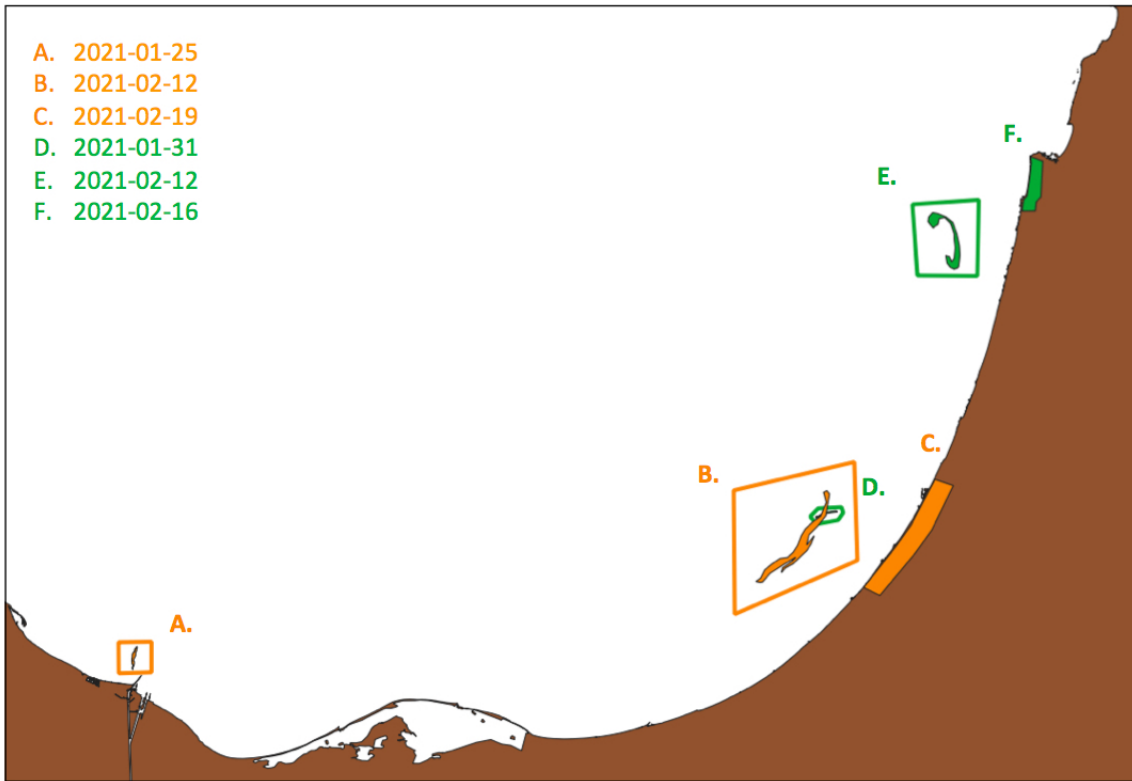


Figure 4. A graphical representation of the spills observed along the coastline of the Eastern Mediterranean and satellite observations matching the sources.

III. RESULTS

The backward-time uncertainty definition provided in Eq. (4), or its analog for the Euclidean distance given by:

$$L_{BUQ}(\mathbf{X}_1, t_1, \tau) = \left[\sum_{i=1}^n |x_i(t_1 - \tau) - x_i^*|^2 \right]^{\frac{1}{2}}, \quad \mathbf{X}_1 \in \mathbb{R}^n, \tau > 0 \quad (5)$$

are very suitable for assessing the performance of ocean models for describing events where the source of a certain observable, for instance, a contaminant, is unknown. This section describes how to implement the use of the definitions

given in (4) or (5) to assess and determine the model that better achieves the observations in a recent oil spill of this type. This event is of a different nature to those described in [6], where after a reported oil spill accident the interest was in describing and controlling its evolution in order to minimize its impact. In contrast, now we are interested in assessing models that provide information about when and where did the spill originate. Good models in the setting described in Figure 1d) are expected to have small distances between \mathbf{X}^* (the blue domain) and \mathbf{x}^* (the target) and we will exploit this idea to measure the quality of available ocean data sets.

We describe next the specific event to be considered under this perspective. At the beginning of 2021, the coastline of several Middle Eastern countries in the Eastern Mediterranean was affected by the presence of oil from an unknown source(s) [10]. No accidents were reported for these spills previous to their arrival at the coast, and therefore there was no hint of their origin. Israeli authorities estimated that more than 1000 tons of tar [11] landed along 180 km of the Israeli and Lebanese shoreline [12–17] in mid-February. They combined the use of satellite images with simulations by Garcia-Sánchez et al. [7], which provided possible sources for this spill. Their work studied this event both from the remote sensing and modeling perspectives. Figure 4 illustrates some affected geographical areas. In this figure, orange and green colors along the coastline mark the oil arrivals. The systematic search of satellite images identified potential sources of these observations and a careful examination concluded that those sources surrounded by green and orange polygons, which correspond to satellite observations, were located in position and time in a manner consistent with the position and dates of the oil that subsequently arrived at the coast. According to [7], orange polygons labeled as A and B, are successive earlier locations to the orange arrival labeled as C. Analogously green polygons labeled as D and E, correspond to the green arrival labeled as F. The successive dates for each observation are given in the figure.

Simulations in [7] demonstrated that the spill was closely following fluid parcel trajectories $\mathbf{x}(t)$ that obeyed the equation:

$$\begin{cases} \frac{d\lambda}{dt} = \frac{u(\lambda, \phi, t)}{R \cos \phi} \\ \frac{d\phi}{dt} = \frac{v(\lambda, \phi, t)}{R} \end{cases} \quad (6)$$

where the position of the fluid parcel at the ocean surface is given in longitude (λ) and latitude (ϕ), and R is the Earth’s radius. The system (6) is the particular form for our study of the general expression given by Eq. (1), where $\mathbf{x} = (\lambda, \phi)$ and its right-hand side represent the two components of the vector field \mathbf{v} , which are determined by the zonal (u) and meridional (v) velocities. These velocity components are obtained as data sets from the Copernicus Marine Monitoring Environmental Service (CMEMS).

Equation (6) is a nonlinear non-autonomous dynamical system in 2D and it is required for implementing the backward evolution of fluid parcels in expression (5). L_{BUQ} in Eq. (5) will have different evaluations for different CMEMS data sets. The goal of this section is to use these outputs to discriminate models. CMEMS provides two data sets describing currents in the Mediterranean Sea. One is the operational Mercator global ocean analysis and forecast system that provides 10 days of 3D global ocean forecasts updated daily. This product includes daily and monthly mean fields of variables such as temperature, salinity, currents, sea level, mixed layer depth, and ice parameters from the top to the bottom of the global ocean. It also includes hourly mean surface fields for sea level height, temperature, and currents. The global ocean output files are displayed with a 1/12 degree horizontal resolution with an equirectangular longitude/latitude projection and 50 vertical levels ranging from 0 to 5500 meters.

The second data set is the physical component of the Mediterranean Forecasting System (Med-Currents), which is a coupled hydrodynamic-wave model, including tides, implemented over the whole Mediterranean Basin, with a higher resolution than the global model. Indeed, its horizontal grid resolution is 1/24 degree with 141 unevenly spaced vertical levels. The model solutions are corrected with a variational data assimilation scheme (3DVAR) of vertical profiles of temperature and salinity along the satellite track that provides observations of sea level anomalies (SLA).

Given that both models provide information for the same area, a natural question is to determine whether one is more suitable than the other for describing transport in the type of event described above. Models such as that given in Eq. (6), possess a transport signature based on invariant manifolds associated with hyperbolic trajectories, which following Poincaré’s idea, constitute geometrical structures on the ocean surface that organize particles schematically by regions corresponding to qualitatively different types of trajectories. These geometrical features allow a more robust analysis of the transport capacity of ocean currents than that based on individual trajectories. Indeed, there exist mathematical results that discuss the persistence of these geometrical structures in the presence of small perturbations, while individual trajectories may be affected much more drastically by perturbations [18, 19]. In the past these features have been used to assess the transport performance of data sets [20–25]. In the context of geophysical flows, these geometrical structures are referred to as Lagrangian Coherent Structures (LCSs). The use of LCS allows a *qualitative* assessment of the performance of data sets, however, definitions such as that given in Eq. (5) allow a *quantitative* analysis that we will implement next in the context of the oil spill event described in [7].

In this work, we compute LCS using Lagrangian Descriptors [26, 27], a method based on computing the function defined as:

$$M(\mathbf{x}_0, t_0, \tau) = \int_{t_0-\tau}^{t_0+\tau} \|\mathbf{v}(\mathbf{x}(\mathbf{x}_0, t), t)\| dt, \quad (7)$$

where the Euclidean norm, $\|\cdot\|$, of the vector field \mathbf{v} is evaluated along fluid parcel trajectories $\mathbf{x}(\mathbf{x}_0, t)$ of Eq. (6), and therefore the integral in Eq. (7) evaluates the arclength of this trajectory on the latitude-longitude plane at the ocean surface. In expression (7), the forward integration from t_0 reveals by means of singular features the stable manifolds associated to hyperbolic trajectories, whereas the backward integration highlights their unstable manifolds. This is explicitly expressed by splitting the integral (7) into two terms as follows:

$$M(\mathbf{x}_0, t_0, \tau) = \int_{t_0-\tau}^{t_0} \mathbf{v}(\mathbf{x}(\mathbf{x}_0, t), t) dt + \int_{t_0}^{t_0+\tau} \mathbf{v}(\mathbf{x}(\mathbf{x}_0, t), t) dt = M^{(b)}(\mathbf{x}_0, t_0, \tau) + M^{(f)}(\mathbf{x}_0, t_0, \tau) \quad (8)$$

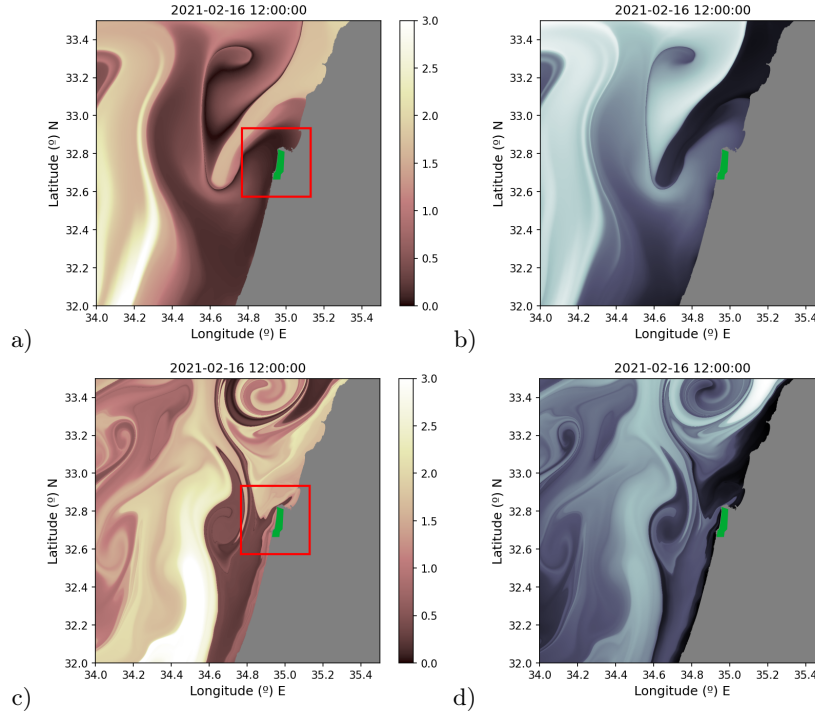


Figure 5. Evaluation on the 16th of February 2021 of L_{BUQ} using the target, $\mathbf{x}^* = (34.36^\circ\text{E}, 31.78^\circ\text{N})$ and of $M^{(b)}$ using $\tau = 16$ days; a) L_{BUQ} with the CMEMS global product; b) $M^{(b)}$ with the CMEMS global product; c) L_{BUQ} with the CMEMS Mediterranean product; d) $M^{(b)}$ with the CMEMS Mediterranean product.

We explore next the implementation of the ideas discussed in the previous section, to evaluate the performance of the two CMEMS products in the context of this environmental damage and their links to the unstable manifolds of hyperbolic trajectories present in the system Eq. (6). Following oil detections displayed in figure 4, we start the discussion considering the first arrival to the coast on the 16th of February 2021, which is the green mark at the Israeli coast (F) and is considered to be the observation \mathbf{x}_1 . For it, we consider that the position (D) on the 31st of January 2021 is its backward time target $\mathbf{x}^* = (34.355734^\circ\text{E}, 31.777414^\circ\text{N})$. Figure 5a) shows the evaluation of L_{BUQ} according to Eq. (5) in a large area, considering that the eastward (u) and northward (v) velocity components are provided by the CMEMS global model. It is remarkable that its structure presents important analogies with the $M^{(b)}$, visible in panel b), which has been computed for $\tau = 16$ days. This image highlights, by means of singular features, the unstable manifolds of hyperbolic trajectories present in the vector field supplied by Eq. (6). This result confirms that the uncertainty associated with the model has a structure closely related to invariant dynamical structures. The red square in panel a) highlights a neighborhood of the observation whose origin is conjectured to be at target \mathbf{x}^* . This domain \mathbf{X}_1 is used to characterize the performance of the model with respect to the hypothesis, assuming that the model is good if the target is consistent with arrivals in all this domain \mathbf{X}_1 . The model is characterized through

mean values of L_{BUQ} in this box. Panels c) and d) reproduce results for the CMEMS Mediterranean product. It is again clear the close relationship between the structure of L_{BUQ} and the unstable manifolds of hyperbolic trajectories present in Eq. (6).

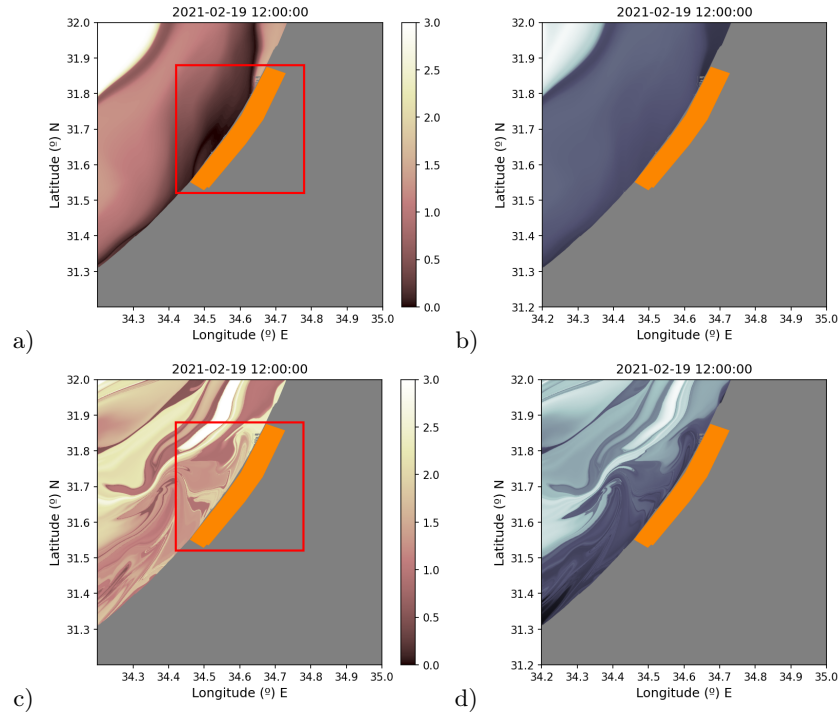


Figure 6. Evaluation on the 19th of February 2021 of L_{BUQ} using the target, $\mathbf{x}^* = (34.32^\circ\text{E}, 31.35^\circ\text{N})$ and of $M^{(b)}$ using $\tau = 25$ days; a) L_{BUQ} with the CMEMS global product; b) $M^{(b)}$ with the CMEMS global product; c) L_{BUQ} with the CMEMS Mediterranean product; d) M^b with the CMEMS Mediterranean product.

We continue the discussion considering that the observation \mathbf{x}_1 is the orange mark at the Gaza coast (C) on the 19th of February 2021. For it, we consider that the position (A) on the 25th of January 2021 is its backward time target: $\mathbf{x}^* = (32.319813^\circ\text{E}, 31.350392^\circ\text{N})$. Figure 6 displays the results both for CMEMS global and Mediterranean products. Panels a) and c) display the outputs of L_{BUQ} , and the red box highlights the neighborhood \mathbf{X}_1 used to characterize the performance of the model. Panels b) and d) again confirm the similarities between the unstable manifolds of hyperbolic trajectories in Eq. (6) and the structure of L_{BUQ} .

It is remarkable that for both cases examined in figures 5 and 6, L_{BUQ} takes, in the neighborhood \mathbf{X}_1 , considerably larger values for the CMEMS Mediterranean product than for the global one. Table I confirms this point by providing the averages in both domains in the column labeled as “Remote Targets”, suggesting the better performance of the global model for these cases.

Figure 4 shows that related to the oil arrivals marked in green (F) and orange (C), there exist additional targets \mathbf{x}^* nearer and closer to the observation \mathbf{x}_1 , than those previously discussed. These backward-in-time targets, labeled (B) and (E), were identified from satellite imagery between the dates of the original sources and the dates of arrival on shore. These spills, after several days have elapsed since their leak, spread out on the ocean surface due to the ocean movement, which stretches and folds them in a chaotic dynamic. Indeed, this description matches well the appearance of targets (B) and (E), as discussed in [7]. Now we consider the evaluation of L_{BUQ} using these new \mathbf{x}^* to assess both models. We start considering the green observation (F) (\mathbf{x}_1) on the Israeli coast. For it, central coordinates of the spill contour on the 12th of February 2021 are $\mathbf{x}^* = (34.72008^\circ\text{E}, 32.59311^\circ\text{N})$. Other target positions within the extended spill could have been considered, but they do not lead to substantial changes either in the results or in the discussions. Panels a) and b) in figure 7 display the evaluation L_{BUQ} for this target, considering the CMEMS global and Mediterranean products respectively. Regarding the orange observation (C) coordinates that correspond to its backward-in-time target on the 12th of February 2021 are $\mathbf{x}^* = (34.2891^\circ\text{E}, 32.59311^\circ\text{N})$. As before, given that this is a rather spread contour, other target positions could have been considered, but we do not discuss them as they provide no changes in the conclusions. For these assumptions panels c) and d) of figure 7 display L_{BUQ} considering the CMEMS global and Mediterranean products respectively. In these pictures, the red box delimits the boundaries

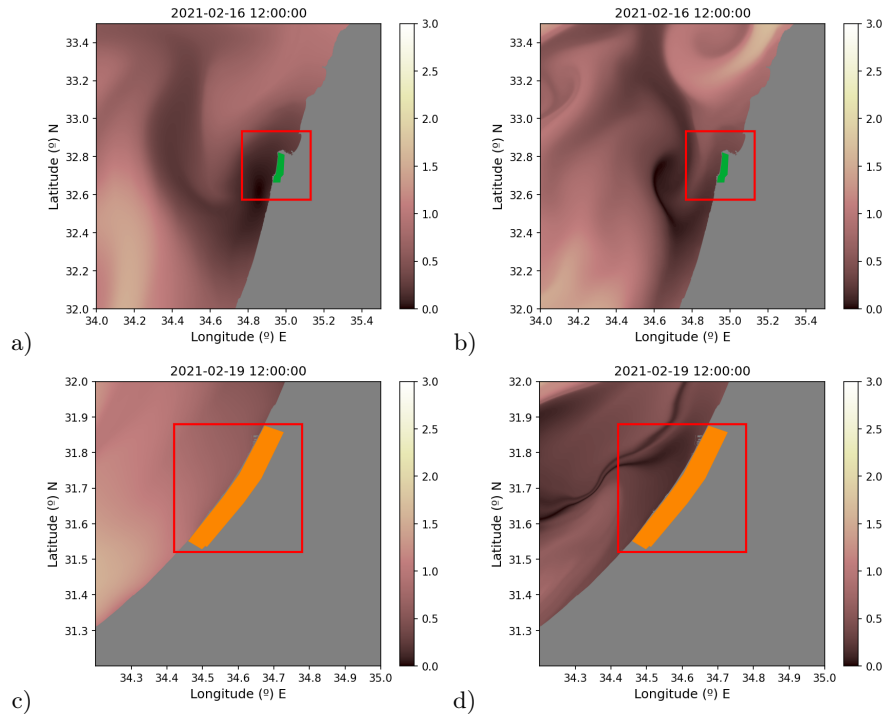


Figure 7. Evaluation L_{BUQ} on the Israel and Gaza coast for the close targets using the global and the Mediterranean data. L_{BUQ} on 16th of February 2021 using the target, $\mathbf{x}^* = (34.72^\circ\text{E}, 32.59^\circ\text{N})$; a) L_{BUQ} on the Israel coast with the CMEMS global product; b) $M^{(b)}$ on the Israel coast with the CMEMS Mediterranean product. L_{BUQ} on 19th of February 2021 using the target, $\mathbf{x}^* = (34.28^\circ\text{E}, 32.59^\circ\text{N})$; c) L_{BUQ} on the Gaza coast with the CMEMS Global product; d) $M^{(b)}$ on the Gaza coast with the CMEMS Mediterranean product.

of the neighborhood \mathbf{X}_1 used to evaluate the model performance. In this case the column ‘‘Close Targets’’ in Table I shows the results for both models.

A discussion of these results requires highlighting the sizes involved in the different settings. The distance between the remote targets and the Gaza (orange) and Israeli (green) shore impact points are, respectively, ~ 215 km and 127 km. These size ranges involve ocean mesoscale structures, which seem to be better represented in the global model. The close targets are at distances ~ 28 km and 33 km respectively of the Gaza and Israel arrival points (C) and (F). These sizes involve ocean submesoscale structures, which should be better represented by the higher resolution model, which is the CMEMS Mediterranean product. Indeed, this is the one that on average performs better for the closer targets, although the global model shows a good performance as well for the Israel case, despite its lower resolution.

| | Remote Targets | | Close Targets | |
|--------|----------------|---------------|---------------|---------------|
| Case | Global | Mediterranean | Global | Mediterranean |
| Israel | 0.2989 | 0.9434 | 0.1642 | 0.3375 |
| Gaza | 0.34074 | 1.5426 | 0.7810 | 0.24666 |

Table I. Averages of L_{BUQ} within the \mathbf{X}_1 domains highlighted with red boxes.

IV. CONCLUSIONS

This article proposes a new definition for uncertainty quantification that extends those recently proposed in oceanic contexts in [6, 28]. The new definition is referred to as Lagrangian Uncertainty Quantification in Backward time (L_{BUQ}), and it is suited to measure if a given transport model consistently describes the source of an observation whose origin is unknown.

We have found that the defined quantity L_{BUQ} , when evaluated in the neighborhood of an observation with respect to its backward-in-time target, has a *structure* which has been linked to the unstable invariant manifolds of the hyperbolic trajectories present in the model vector field. This link has been rigorously proven in a simple example, and numerically verified in a real inspired case: the oil spill accident that affected the Eastern Mediterranean in 2021, which was studied in [7].

The new definition, L_{BUQ} , has been exploited to quantify the performance of different CMEMS products to describe the sequence of events reported in [7] regarding the oil spill accident in the Eastern Mediterranean in 2021. In this event, some of the backward-in-time targets are very far from the impact point, and their evolution involves mesoscale structures, which our analysis shows are better represented in the CMEMS global model. On the contrary for targets that are close, involving submesoscale structures, on average the CMEMS Mediterranean product performs better, although in some cases CMEMS global product also performs well.

Our results are set within a different framework compared to other inverse uncertainty studies. In those studies, the model typically consists of a dissipative partial differential equation with adjustable parameters, and the uncertainty analysis aims to determine the best-fitting parameters based on observations. However, in our framework, the model comprises a two-dimensional set of volume-preserving (non-dissipative) non-autonomous differential equations, and their exact form is unknown as they rely on approximated velocity fields. Many classical inverse problems, such as the inverse heat equation, are ill-posed, meaning that inferring a previous temperature distribution from final data is highly sensitive to changes in the final data. Although our framework differs from such cases, we still observe a high sensitivity to the uncertainty measured around a final observation, as demonstrated in Figures 5-7. In the neighborhood surrounding the final observation, the uncertainty exhibits a complex structure with high oscillations, and we have established a connection with the unstable manifolds of hyperbolic trajectories. Thus, we illustrate how concepts from dynamical systems are linked to uncertainty quantification, whereas a statistical perspective has traditionally been the main focus in this context. Finally, we have shown how to implement these concepts for the practical purpose of discriminating the best data set performer on specific environmental applications.

ACKNOWLEDGEMENTS

GGs and AMM acknowledge the support of a CSIC PIE project Ref. 202250E001. AMM, GGS and MA acknowledge the support from grant PID2021-123348OB-I00 funded by MCIN/ AEI /10.13039/501100011033/ and by FEDER A way to making Europe. MA acknowledges the support from the grant CEX2019-000904-S and IJC2019-040168-I funded by: MCIN/AEI/10.13039/501100011033. AMM, GGS, and MA are active members of the CSIC Interdisciplinary Thematic Platforms TELEDETECT. SW gratefully acknowledges the support of the William R. Davis '68 Chair at the United States Naval Academy and the support of EPSRC Grant No. EP/P021123/1.

APPENDIX

Our proof follows the spirit of the work by [28–31]. We assume the definition of singular features given there, by considering that these are features of L_{BUQ} (we consider for simplicity the expression for L_{BUQ} given in Eq. 4) on which the transversal derivative is not defined. We prove that, for the simple case of the linear saddle, the unstable manifold of the hyperbolic fixed point is aligned with singular features of L_{BUQ} .

We study the vector field of the autonomous saddle case, where the equations of motion are the following:

$$\begin{cases} \frac{dx}{dt} = \lambda x, \\ \frac{dy}{dt} = -\lambda y, \end{cases} \quad \lambda > 0 \quad (9)$$

The system has a unique solution for a given condition (x_1, y_1) at time $t = t_1$:

$$\begin{cases} x(t) = x_1 e^{\lambda(t-t_1)} \\ y(t) = y_1 e^{-\lambda(t-t_1)}, \end{cases} \quad \lambda > 0 \quad (10)$$

Notice that the origin $(0, 0)$ is a hyperbolic fixed point with stable and unstable manifolds which are the following:

$$W^s(0, 0) = \{(x, y) \in \mathbb{R}^2 : x = 0, y \neq 0\}, \quad (11)$$

$$W^u(0,0) = \{(x,y) \in \mathbb{R}^2 : x \neq 0, y = 0\}, \quad (12)$$

Since in this paper we study the backwards uncertainty quantification method we will consider according to (4):

$$\begin{aligned} L_{BUQ}(\mathbf{X}_1, t_1, \tau, p) &= \sum_{i=1}^n |x_i(t_1 - \tau) - x_i^*|^p \\ &= |x_1 e^{\lambda \tilde{t}} - x^*|^p + |y_1 e^{-\lambda \tilde{t}} - y^*|^p \\ &= |x_1|^p |\omega - a|^p + |y_1|^p \omega^{-p} |1 - b\omega|^p \end{aligned} \quad (13)$$

where $\tilde{t} = t_1 - \tau - t_1 = -\tau < 0$, $a = \frac{x^*}{x_1}$, $b = \frac{y^*}{y_1}$ and $\omega = e^{\lambda \tilde{t}} = e^{-\lambda \tau}$, $p \leq 1$. In order to compute equation (13) we will calculate, for simplicity, each of the terms separately. In the first term we notice that the sign of the expression $(\omega - a)$, for $\tau \gg 1$, will be positive when $a < 0$ and could be negative when $a > 0$.

- For $a < 0$:

$$|\omega - a|^p = (\omega - a)^p \quad (14)$$

$$= (-a)^p + p\omega(-a)^{p-1} + \frac{1}{2}(p-1)p\omega^2(-a)^{p-2} + \frac{1}{6}(p-2)(p-1)p\omega^3(-a)^{p-3} + O(\omega^4) \quad (15)$$

$$= (-a)^p + O(e^{-\lambda \tau}), e^{-\lambda \tau} \ll 1 \quad (16)$$

- For $a > 0$ let be t_L such that for $\tau > t_L$, we get that $(\omega - a) < 0$:

$$|\omega - a|^p = (-\omega + a)^p = a^p + p\omega a^{p-1} + \frac{1}{2}(p-1)p\omega^2 a^{p-2} + \frac{1}{6}(p-2)(p-1)p\omega^3 a^{p-3} + O(\omega^4) \quad (17)$$

$$= a^p + O(\omega) \quad (18)$$

Therefore

$$|\omega - a|^p = |a|^p + O(e^{-\lambda \tau}), \omega \ll 1. \quad (19)$$

Note that $a = x^*/x_1$. Thus

$$|x_1|^p |\omega - a|^p = |x_1|^p |e^{-\lambda \tau} - a|^p = |x^*|^p + O(|x_1|^p e^{-\lambda \tau}), e^{-\lambda \tau} \ll 1.$$

For the factor $|1 - b\omega|^p$ of the second term there exists a t_L such that if $\tau > t_L$, then $b\omega \ll 1$ and $(1 - b\omega) > 0$. This is always the case for $b < 0$ and is a plausible assumption for $b > 0$, if $b \ll \omega^{-1}$. We recall that $b = y^*/y_1$ and that therefore such t_L exists if $y_1 \neq 0$. In this case positiveness is guaranteed for sufficiently large τ , i.e., a Taylor series around $\omega = 0$, attained if $\tau \gg 1$ and $\tau > t_L$, is performed for the binomial:

$$(1 - b\omega)^p = 1 - bp\omega + \frac{1}{2}b^2(p-1)p\omega^2 - \frac{1}{6}\omega^3 (b^3(p-2)(p-1)p) + O(\omega^4).$$

Therefore,

$$\frac{1}{\omega^p} (1 - b\omega)^p = \omega^{-p} - bp\omega^{(1-p)} + \frac{1}{2}b^2(p-1)p\omega^{(2-p)} - O(\omega^{(3-p)}).$$

Finally we get:

$$|y_1|^p \omega^{-p} |1 - b\omega|^p = |y_1|^p |\omega^{-p} - b|^p \quad (20)$$

$$= |y_1|^p |e^{\lambda \tau p} - b|^p \quad (21)$$

$$= |y_1|^p e^{\lambda \tau p} + O(|y_1|^p b e^{-\lambda \tau (1-p)}) \quad (22)$$

Thus, we can approximate L_{BUQ} as

$$L_{BUQ}(\mathbf{X}_1, t_1, \tau, p) \approx |x^*|^p + |y_1 e^{\lambda \tau}|^p = |x^*|^p + |y_1|^p e^{\lambda \tau p} \quad (23)$$

the dominant term is the term $|y_1|^p e^{\lambda \tau p}$. Therefore the unstable manifold at $y = 0$, for ‘sufficiently large’ τ , is aligned with a singular feature of L_{BUQ} , as long as $y_1 \neq 0$, and for any $|y_1| > 0$ for a sufficient large τ satisfying, $\tau > t_L$.

DECLARATION OF GENERATIVE AI AND AI-ASSISTED TECHNOLOGIES IN THE WRITING PROCESS

During the preparation of this work, AMM, MA used Google Translator, Grammarly, and Chat GPT to improve the use of English in writing. After using these tools/services, AMM, MA reviewed and edited the content as necessary and take full responsibility for the content of the publication.

-
- [1] X. Wu, T. Kozłowski, H. Meidani, K. Shirvan, Inverse uncertainty quantification using the modular bayesian approach based on gaussian process, part 2: Application to trace, *Nuclear Engineering and Design* 335 (2018) 417–431.
 - [2] P. Domitr, M. Włostowski, R. Laskowski, R. Jurkowski, Comparison of inverse uncertainty quantification methods for critical flow test, *Energy* (2022) 125640.
 - [3] A. de Crècy, Determination of the uncertainties of the constitutive relationships in the CALTHARE 2 code, Technical Report, American Society of Mechanical Engineers, New York, NY (United States), 1996.
 - [4] A. Petruzzi, The casualidad method for uncertainty evaluation of best-estimate system thermal-hydraulic calculations, *Nuclear Technology* 205 (2019) 1554–1566.
 - [5] G. García-Sánchez, A. Mancho, S. Wiggins, A bridge between invariant dynamical structures and uncertainty quantification, *Commun Nonlinear Sci Numer Simulat* 104 (2022) 106016. doi:doi:10.1016/j.cnsns.2021.106016.
 - [6] G. García-Sánchez, A. M. Mancho, A. G. Ramos, J. Coca, B. Pérez-Gómez, E. Álvarez-Fanjul, M. G. Sotillo, M. García-León, V. J. García-Garrido, S. Wiggins, Very high resolution tools for the monitoring and assessment of environmental hazards in coastal areas, *Frontiers in Marine Science* 7 (2021).
 - [7] G. García-Sánchez, A. M. Mancho, R. A. G., C. J., S. Wiggins, Structured pathways in the turbulence organizing recent oil spill events in the eastern mediterranean, *Scientific Reports* 12 (2022) 3662.
 - [8] B. A. Brushett, B. A. King, C. Lemckert, Evaluation of met-ocean forecast data effectiveness for tracking drifters deployed during operational oil spill response in australian waters, *Journal of Coastal Research* (2011) 991–994.
 - [9] X. Zhang, L. Cheng, F. Zhang, J. Wu, S. Li, J. Liu, S. Chu, N. Xia, K. Min, X. Zuo, et al., Evaluation of multi-source forcing datasets for drift trajectory prediction using lagrangian models in the south china sea, *Applied Ocean Research* 104 (2020) 102395.
 - [10] Wikipedia, 2021 Mediterranean Oil Spill., Wikipedia, https://en.wikipedia.org/wiki/2021_Mediterranean_oil_spill, 2021.
 - [11] Z. Rinat and A. Ben Zikri, Oil Spill Off Israel's Coast Is Its Worst Maritime Pollution in Decades, and Cleanup 'Could Take Years', *Haaretz*, <https://www.haaretz.com/israel-news/.premium-oil-spill-off-israel-s-coast-is-its-worst-maritime-pollution-in-decades-1.9553528>, 2021.
 - [12] R. Tercatin, Damage to Israeli marine environment from tar spill extreme, experts say, *Jerusalem Post*, <https://www.jpost.com/israel-news/damage-to-israeli-marine-environment-from-tar-spill-extreme-experts-say-659716>, 2021.
 - [13] M. Kaplan-Zantopp, Israel oil spill: How did it happen and what will we do going forward?, *Jerusalem Post*, <https://www.jpost.com/israel-news/israel-oil-spill-how-did-it-happen-and-what-will-we-do-going-forward-660242>, 2021.
 - [14] T. Joffre and R. Tercatin, Israel investigates tar spill calamity, places inquiry under gag order, *Jerusalem Post*, <https://www.jpost.com/israel-news/israel-oil-spill-disaster-investigation-details-placed-under-censor-659765>, 2021.
 - [15] AL JAZEERA AND NEWS AGENCIES, Lebanon begins cleaning beaches after oil spill, *Aljazeera*, <https://www.aljazeera.com/news/2021/2/27/lebanon-begins-cleaning-beaches-after-oil-spill>, 2021.
 - [16] Rutgers Staff, Oil spill off Israel reaches south Lebanese beaches, *Rutgers*, <https://www.reuters.com/article/us-israel-environment-oil-spill-lebanon-idUSKBN2AM19V>, 2021.
 - [17] A. Polidura, Israel's oil spill now affects entire Lebanese coastline, *Atalayar*, <https://atalayar.com/en/content/israels-oil-spill-now-affects-entire-lebanese-coastline>, 2021.
 - [18] V. J. García-Garrido, J. Curbelo, A. M. Mancho, S. Wiggins, C. R. Mechoso, The application of lagrangian descriptors to 3d vector fields, *Regul Chaotic Dyn* 23 (2018) 551–568. doi:doi:10.1134/S1560354718050052.
 - [19] G. Haller, Lagrangian coherent structures from approximate velocity data., *Phys. Fluids* 14 (2002) 1851–1861.
 - [20] L. Kuznetsov, M. Toner, A. D. Kirwan, C. K. R. T. Jones, L. H. Kantha, J. Choi, The Loop Current and adjacent rings delineated by Lagrangian analysis of the near-surface flow, *J. Mar. Res.* 60 (2002) 405–429.
 - [21] S. C. Shadden, F. Lekien, J. D. Paduan, F. P. Chavez, J. E. Marsden, The correlation between surface drifters and coherent structures based on high-frequency radar data in Monterey Bay, *Deep Sea Res. II* 56 (2009) 161–172.
 - [22] A. C. Haza, A. Griffa, P. Martin, A. Molcard, T. M. Özgökmen, A. Poje, R. Barbanti, J. Book, P. Poulain, M. Rixen, P. Zanasca, Model-based directed drifter launches in the Adriatic Sea: Results from the DART experiment, *Geophys. Res. Lett* 34 (2007) L10605.
 - [23] A. C. Haza, T. Özgökmen, A. Griffa, A. Molcard, P. M. Poulain, G. Peggion, Transport properties in small-scale coastal flows: relative dispersion from VHF radar measurements in the Gulf of La Spezia, *Ocean Dynam.* 60 (2010) 861–882.
 - [24] C. Mendoza, A. Mancho, S. Wiggins, Lagrangian descriptors and the assessment of the predictive capacity of oceanic data sets, *Nonlinear Processes in Geophysics* 21 (2014) 677–689.
 - [25] V. J. Garcia-Garrido, A. M. Mancho, S. Wiggins, C. Mendoza, A dynamical systems approach to the surface search for debris associated with the disappearance of flight MH370., *Nonlin. Processes Geophys.* 22 (2015) 701–712. doi:doi:

10.5194/npg-22-701-2015.

- [26] C. Mendoza, A. M. Mancho, Hidden geometry of ocean flows, *Phys Rev Lett* 105 (2010) 038501. doi:doi:10.1103/PhysRevLett.105.038501.
- [27] A. M. Mancho, S. Wiggins, J. Curbelo, C. Mendoza, Lagrangian descriptors: A method for revealing phase space structures of general time dependent dynamical systems, *Commun. Nonlinear Sci. Numer. Simul.* 18 (2013) 3530–3557. doi:doi:https://doi.org/10.1016/j.cnsns.2013.05.002.
- [28] G. García-Sánchez, A. M. Mancho, S. Wiggins, A bridge between invariant dynamical structures and uncertainty quantification, *Commun. Nonlinear Sci. Numer. Simul.* 104 (2022).
- [29] C. Lopesino, F. Balibrea-Iniesta, V. J. García-Garrido, S. Wiggins, A. M. Mancho, A theoretical framework for lagrangian descriptors, *International Journal of Bifurcation and Chaos* 27 (2017) 1730001.
- [30] C. Lopesino, F. Balibrea, S. Wiggins, A. M. Mancho, Lagrangian descriptors for two dimensional, area preserving, autonomous and nonautonomous maps, *Communications in Nonlinear Science and Numerical Simulation* 27 (2015) 40–51.
- [31] V. J. García-Garrido, F. Balibrea-Iniesta, S. Wiggins, A. M. Mancho, C. Lopesino, Detection of phase space structures of the cat map with lagrangian descriptors, *Regular and Chaotic Dynamics* 23 (2018) 751–766.